LETTER

doi:10.1038/nature14889

Spawning rings of exceptional points out of Dirac cones

Bo Zhen[1]*, Chia Wei Hsu[1,2]*, Yuichi Igarashi[1,3]*, Ling Lu[1], Ido Kaminer[1], Adi Pick[1,4], Song-Liang Chua[5], John D. Joannopoulos[1] & Marin Soljačić[1]

The Dirac cone underlies many unique electronic properties of graphene[1] and topological insulators, and its band structure—two conical bands touching at a single point—has also been realized for photons in waveguide arrays[2], atoms in optical lattices[3], and through accidental degeneracy[4,5]. Deformation of the Dirac cone often reveals intriguing properties; an example is the quantum Hall effect, where a constant magnetic field breaks the Dirac cone into isolated Landau levels. A seemingly unrelated phenomenon is the exceptional point[6,7], also known as the parity–time symmetry breaking point[8–11], where two resonances coincide in both their positions and widths. Exceptional points lead to counter-intuitive phenomena such as loss-induced transparency[12], unidirectional transmission or reflection[11,13,14], and lasers with reversed pump dependence[15] or single-mode operation[16,17]. Dirac cones and exceptional points are connected: it was theoretically suggested that certain non-Hermitian perturbations can deform a Dirac cone and spawn a ring of exceptional points[18–20]. Here we experimentally demonstrate such an 'exceptional ring' in a photonic crystal slab. Angle-resolved reflection measurements of the photonic crystal slab reveal that the peaks of reflectivity follow the conical band structure of a Dirac cone resulting from accidental degeneracy, whereas the complex eigenvalues of the system are deformed into a two-dimensional flat band enclosed by an exceptional ring. This deformation arises from the dissimilar radiation rates of dipole and quadrupole resonances, which play a role analogous to the loss and gain in parity–time symmetric systems. Our results indicate that the radiation existing in any open system can fundamentally alter its physical properties in ways previously expected only in the presence of material loss and gain.

Closed and lossless physical systems are described by Hermitian operators, which guarantee realness of the eigenvalues and a complete set of eigenfunctions that are orthogonal to each other. On the other hand, systems with open boundaries[7,21] or with material loss and gain[9–17,19] are non-Hermitian[6], and have non-orthogonal eigenfunctions with complex eigenvalues where the imaginary part corresponds to decay or growth. The most drastic difference between Hermitian and non-Hermitian systems is that the latter exhibit exceptional points (EPs) where both the real and the imaginary parts of the eigenvalues coalesce. At an EP, two (or more) eigenfunctions collapse into one so the eigenspace no longer forms a complete basis, and this eigenfunction becomes orthogonal to itself under the unconjugated 'inner product'[6,7]. To date, most studies of the EP and its intriguing consequences concern parity–time symmetric systems that rely on material loss and gain[9–17,19], but EPs are a general property that require only non-Hermiticity. Here, we show the existence of EPs in a photonic crystal slab with negligible absorption loss and no artificial gain. When a Dirac-cone system has dissimilar radiation rates, the band structure is altered abruptly to show branching features with a ring of EPs. We provide a complete picture of this system, ranging from an analytic model and numerical simulations to experimental observations; taken together, these results illustrate the role of radiation-induced non-Hermiticity that bridges the study of EPs and the study of Dirac cones.

We start by showing that non-Hermiticity from radiation can deform an accidental Dirac point into a ring of EPs. First, consider a two-dimensional photonic crystal (Fig. 1a inset), where a square lattice (periodicity a) of circular air holes (radius r) is introduced in a dielectric material. This is a Hermitian system, as there is no material gain or loss and no open boundary for radiation. By tuning a system parameter (for example, r), one can achieve accidental degeneracy between a quadrupole mode and two degenerate dipole modes at the Γ point (centre of the Brillouin zone), leading to a linear Dirac dispersion due to the anti-crossing between two bands with the same symmetry[4,22]. The accidental Dirac dispersion from the effective Hamiltonian model (see equation (1) below with $\gamma_d = 0$) is shown as solid lines in Fig. 1a, agreeing with numerical simulation results (symbols). In the effective Hamiltonian we do not consider the dispersionless third band (grey line) owing to symmetry arguments (Supplementary Information section I), although this third band cannot be neglected in certain calculations, including the Berry phase and effective medium properties[23].

Next, we consider a similar, but open, system: a photonic crystal slab (Fig. 1b inset) with finite thickness h. With the open boundary, modes within the radiation continuum become resonances because they radiate by coupling to extended plane waves in the surrounding medium. Non-Hermitian perturbations need to be included in the Hamiltonian to account for the radiation loss. To the leading order, radiation of the dipole mode can be described by adding an imaginary part $-i\gamma_d$ to the Hamiltonian, while the quadrupole mode does not radiate owing to its symmetry mismatch with the plane waves[24]. Specifically, at the Γ point the system has C_2 rotational symmetry (invariant under 180° rotation around the z axis), and the quadrupole mode does not couple to the radiating plane wave because the former has a field profile $\boldsymbol{E}(\boldsymbol{r})$ that is even under C_2 rotation, $\boldsymbol{E}(\boldsymbol{r}) = \hat{O}_{C_2}\boldsymbol{E}(\boldsymbol{r})$, whereas the latter is odd, $\boldsymbol{E}(\boldsymbol{r}) = -\hat{O}_{C_2}\boldsymbol{E}(\boldsymbol{r})$. The effective Hamiltonian is

$$H_{\mathrm{eff}} = \begin{pmatrix} \omega_0 & v_g|\boldsymbol{k}| \\ v_g|\boldsymbol{k}| & \omega_0 - i\gamma_d \end{pmatrix} \quad (1)$$

with complex eigenvalues

$$\omega_{\pm} = \omega_0 - i\frac{\gamma_d}{2} \pm v_g\sqrt{|\boldsymbol{k}|^2 - k_c^2} \quad (2)$$

where ω_0 is the frequency at accidental degeneracy, v_g is the group velocity of the linear Dirac dispersion in the absence of radiation, $|\boldsymbol{k}|$ is the magnitude of the in-plane wavevector (k_x, k_y), and $k_c \equiv \gamma_d/2v_g$. Here, one of the three bands is decoupled from the other two and is not included in equation (1) (see Supplementary Information section II). In equation (2), a ring defined by $|\boldsymbol{k}| = k_c$ separates the k space

[1]Research Laboratory of Electronics, Massachusetts Institute of Technology, Cambridge, Massachusetts 02139, USA. [2]Department of Applied Physics, Yale University, New Haven, Connecticut 06520, USA. [3]Smart Energy Research Laboratories, NEC Corporation, 34 Miyuiga-ka, Tsukuba, Ibaraki 305-8501, Japan. [4]Department of Physics, Harvard University, Cambridge, Massachusetts 02138, USA. [5]DSO National Laboratories, 20 Science Park Drive, Singapore 118230, Singapore.

*These authors contributed equally to this work.

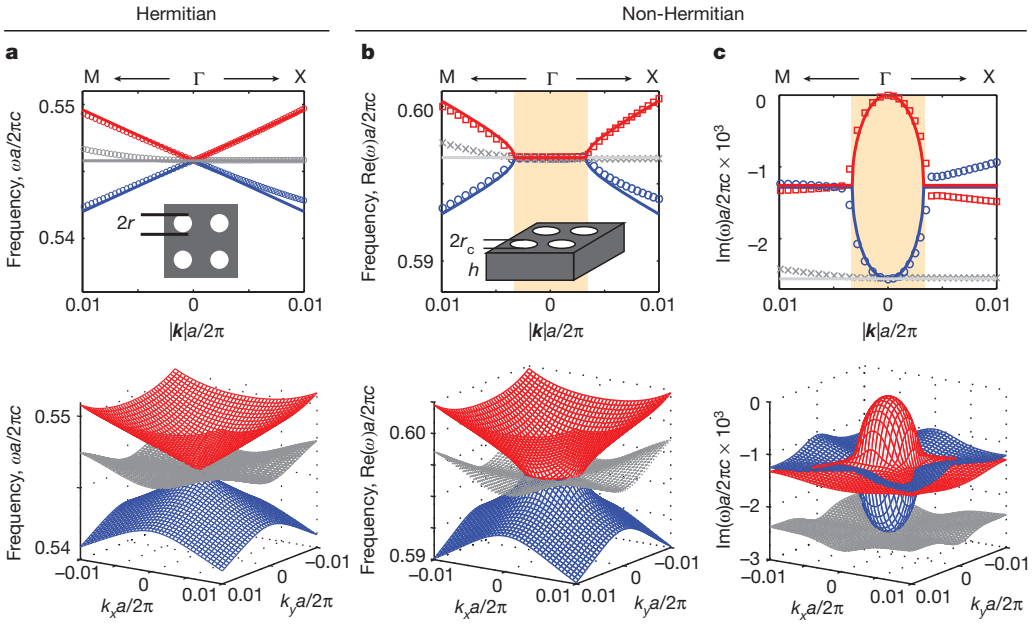

Figure 1 | Accidental degeneracy in Hermitian and non-Hermitian photonic crystals. **a**, Band structure of a two-dimensional photonic crystal consisting of a square lattice of circular air holes. Tuning the radius r leads to accidental degeneracy between a quadrupole band and two doubly degenerate dipole bands, resulting in two bands with linear Dirac dispersion (red and blue) and a flat band (grey). **b**, **c**, The real (**b**) and imaginary (**c**) parts of the eigenvalues of an open, and therefore non-Hermitian, system: a photonic crystal slab with finite thickness, h. By tuning the radius, accidental degeneracy in the real part can be achieved, but the Dirac dispersion is deformed owing to the non-Hermiticity. The analytic model predicts that the real (imaginary) part of the eigenvalue stays as a constant inside (outside) a ring in the wavevector space, indicating two flat bands in dispersion, with a ring of exceptional points (EPs) where both the real and the imaginary parts are degenerate. The orange shaded regions correspond to the inside of the ring. In the upper panels of **a**–**c**, solid lines are predictions from the analytic model and symbols are from numerical simulations: red squares represent the band connecting to the quadrupole mode at the centre; blue circles represent the band connecting to the dipole mode at the centre; and grey crosses represent the third band that is decoupled from the previous two due to symmetry. The three-dimensional plots in the lower panels are from simulations.

into two regions: inside the ring ($|\boldsymbol{k}| < k_c$), $\mathrm{Re}(\omega_\pm)$ are dispersionless and degenerate; outside the ring ($|\boldsymbol{k}| > k_c$), $\mathrm{Im}(\omega_\pm)$ are dispersionless and degenerate. In the vicinity of k_c, $\mathrm{Im}(\omega_\pm)$ and $\mathrm{Re}(\omega_\pm)$ exhibit square-root dispersion (also known as branching behaviour[6]) inside and outside the ring, respectively. Exactly on the ring ($|\boldsymbol{k}| = k_c$), the two eigenvalues $\omega_\pm$ are degenerate in both real and imaginary parts; meanwhile, the matrix H_{eff} becomes defective with an incomplete eigenspace spanned by only one eigenvector $(1, -i)^{\mathrm{T}}$ that is orthogonal to itself under the unconjugated 'inner product', given by $\boldsymbol{a}^{\mathrm{T}}\boldsymbol{b}$ for vectors $\boldsymbol{a}$ and $\boldsymbol{b}$. This self-orthogonality is the definition of EPs; hence, here we have not just one EP, but a continuous ring of EPs. We call it an exceptional ring.

Figure 1b, c shows the complex eigenvalues of the photonic crystal slab structure calculated numerically (symbols), which closely follow the analytic model of equation (2) shown as solid lines in the figure. In Supplementary Fig. 1, we show that the two eigenvectors indeed coalesce into one at the EP, which is impossible in Hermitian systems (also see Supplementary Information section III). When the radius r of the holes is tuned away from accidental degeneracy, the exceptional ring and the associated branching behaviour disappear, as shown in Supplementary Fig. 2. Several properties of the photonic crystal slab contribute to the existence of this exceptional ring. Owing to periodicity, one can probe the dispersion from two degrees of freedom, k_x and k_y, in just one structure. The open boundary provides radiation loss, and the C_2 rotational symmetry differentiates the radiation loss of the dipole mode and of the quadrupole mode.

We can rigorously show that the exceptional ring exists in realistic photonic crystal slabs, not just in the effective Hamiltonian model. Our proof is based on the unique topological property of EPs: when the system parameters evolve adiabatically along a loop encircling an EP, the two eigenvalues switch their positions when the system returns to its initial parameters[7,21,25], in contrast to the typical case where the two eigenvalues return to themselves. Using this property, we numerically show, in Supplementary Fig. 3 and Supplementary Information section IV, that the complex eigenvalues always switch their positions along every direction in the k space, and therefore prove the existence of this exceptional ring. As opposed to the simplified effective Hamiltonian model, in a real photonic crystal slab, the EP may exist at a slightly different magnitude of k and for a slightly different hole radius r along different directions in the k space, but this variation is small and negligible in practice (Supplementary Information section V).

To demonstrate the existence of the exceptional ring in such a system, we fabricate large-area periodic patterns in a Si_3N_4 slab ($n = 2.02$ in the visible spectrum, thickness 180 nm) on top of 6 μm of silica ($n = 1.46$) using interference photolithography[24]. Scanning electron microscope (SEM) images of the sample are shown in Fig. 2a, featuring a square lattice (periodicity $a = 336$ nm) of cylindrical air holes with radius 109 nm. We immerse the structure into an optical liquid with a specified refractive index that can be tuned; accidental degeneracy in the Hermitian part is achieved when the liquid index is selected to be $n = 1.48$. We perform angle-resolved reflectivity measurements (set-up shown in Fig. 2b) between 0° and 2° along the $\Gamma \rightarrow \mathrm{X}$ direction and the $\Gamma \rightarrow \mathrm{M}$ direction, for both s and p polarizations. Details of the sample fabrication and the experimental setup can be found in Supplementary Information section VI. The measured reflectivity for the relevant polarization is plotted in the upper panel of Fig. 2c, showing good agreement with numerical simulation results (lower panel), with differences coming from scattering due to surface roughness, inhomogeneous broadening, and the uncertainty in the measurements of system parameters. The complete experimental result for both polarizations is shown in Supplementary Fig. 4; the third and dispersionless band shows up in the other polarization, decoupled from the two bands of interest.

The peaks of reflectivity (dark red colour in Fig. 2c) follow the linear Dirac dispersion; this feature disappears for structures with different radii that do not reach accidental degeneracy (experimental results in

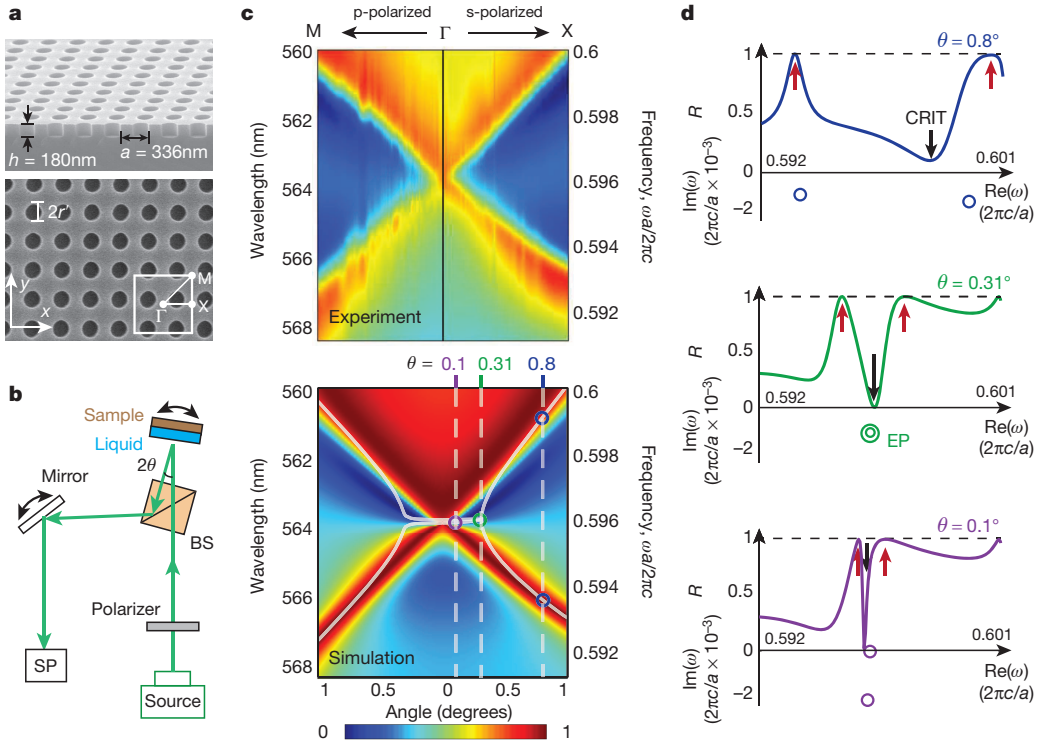

Figure 2 | Experimental reflectivity spectrum and accidental Dirac dispersion. **a**, SEM images of the photonic crystal samples: side view (upper panel) and top view (lower panel). **b**, Schematic drawing of the measurement set-up. Linearly polarized light from a super-continuum source is reflected off the photonic crystal slab ('sample') immersed in an optical liquid, and collected by a spectrometer (SP). The incident angle θ is controlled using a precision rotating stage. BS, beam splitter. **c**, Reflectivity spectrum of the sample measured experimentally (upper panel) and calculated numerically (lower panel) along the $\Gamma \rightarrow$ X and the $\Gamma \rightarrow$ M directions. The peak location of reflectivity reveals the Hermitian part of the system, which forms Dirac dispersion due to accidental degeneracy. In the lower panel, white solid lines indicate the real part of the eigenvalues; spectra and eigenvalues at three representative angles (marked by dashed lines and circles) are shown in **d**. **d**, Three line cuts of reflectivity R from simulation results. Also shown are the complex eigenvalues (open circles) calculated numerically. At large angles (0.8°), the two resonances are far apart, so the reflectivity peaks (red arrows) are close to the actual positions of the complex eigenvalues. However, at small angles (0.3°, 0.1°), the coupling between resonances cause the resonance peaks (red arrows) to have much greater separations in frequency compared to the complex eigenvalues. The black arrows mark the dips in reflectivity that correspond to the coupled-resonator induced transparency (CRIT, see text for details).

Supplementary Fig. 5). Note that the reflection peaks do not follow the real part of the complex eigenvalues of the Hamiltonian; in fact they follow the eigenvalues of the Hermitian part of the Hamiltonian, even though the Hamiltonian is non-Hermitian. To understand this, we consider a more general two-by-two Hamiltonian of a coupled resonance system H and separate it into a Hermitian part A and an anti-Hermitian part $-iB$ (A and B are both Hermitian)

$$H = \underbrace{\begin{pmatrix} \omega_1 & \kappa \\ \kappa & \omega_2 \end{pmatrix}}_{A} - i\underbrace{\begin{pmatrix} \gamma_1 & \gamma_{12} \\ \gamma_{12} & \gamma_2 \end{pmatrix}}_{iB} \xrightarrow{\text{eigenvalues}} \begin{pmatrix} \omega_+ & 0 \\ 0 & \omega_- \end{pmatrix} \quad (3)$$

As before, we use $\omega_\pm$ to denote the complex eigenvalues of the Hamiltonian $A - iB$. Physically, matrix A describes a lossless system, and matrix $-iB$ adds the effects of loss. In B, the diagonal elements are loss rates (in our system, they come primarily from radiation), and the off-diagonal elements arise from overlap of the two radiation patterns, also known as external coupling of resonances via the continuum. Modelling the reflectivity using temporal coupled-mode theory (TCMT), we show that when matrix B is dominated by radiation, the reflection peaks occur near the eigenvalues $\Omega_{1,2}$ of the Hermitian part A and are independent of the anti-Hermitian part $-iB$ (see Supplementary Information section VII and Supplementary Fig. 6 for details). Therefore, the linear Dirac dispersion observed in the measured data of Fig. 2c (dark red) indicates that we have successfully achieved accidental degeneracy in the eigenvalues of the Hermitian part, consistent with the simplified model in equation (1). In Supplementary Fig. 8b, we plot the values of $\Omega_{1,2}$ extracted from the reflectivity data through a more rigorous data analysis using TCMT (described below); the linear dispersion is indeed observed. We note that when there is substantial non-radiative loss or material gain in the system, the reflection peaks no longer follow the eigenvalues of the Hermitian part (see Supplementary Information section VIII and Supplementary Fig. 7).

The real part of the complex eigenvalues of the Hamiltonian, $\mathrm{Re}(\omega_\pm)$, behave very differently from the reflectivity peaks. Simulation results (solid white lines in the lower panel of Fig. 2c) show $\mathrm{Re}(\omega_\pm)$ is dispersionless at small angles with a branch-point singularity around 0.31°—consistent with the feature predicted by the simplified Hamiltonian in equation (2). In Fig. 2d, we compare the reflectivity spectra from simulations (with peaks indicated by red arrows) with the corresponding complex eigenvalues at three representative angles (0.8° in blue, 0.31° in green and 0.1° in magenta). At 0.31°, the two complex eigenvalues are degenerate, indicating an EP; however, the two reflection peaks do not coincide since they represent the eigenvalues of only the Hermitian part of the Hamiltonian, which does not have degeneracy here. The dip in reflectivity between the two peaks (marked as black arrows in Figs 2 and 3) is the coupled-resonator-induced transparency (CRIT) that arises from the interference between radiation of the two resonances[26], similar to electromagnetically induced transparency.

Qualitatively, the peak locations of the measured reflectivity spectrum reveal the eigenvalues of the Hermitian part, A, and the linewidths of the peaks reveal the anti-Hermitian part, $-iB$; diagonalizing $A - iB$ yields the eigenvalues $\omega_\pm$, as illustrated in equation (3). To be more quantitative, we use TCMT and account for both the direct

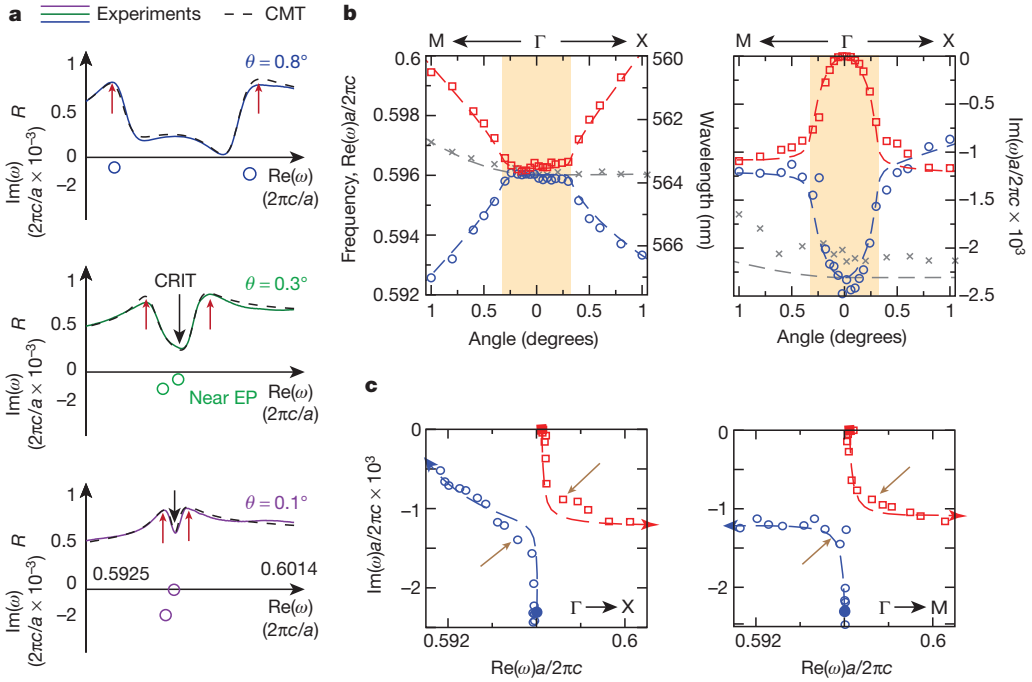

Figure 3 | Experimental demonstration of an exceptional ring. **a**, Examples of reflection spectrum R from the sample at three different angles (0.8° blue, 0.3° green and 0.1° magenta, solid lines) measured with s-polarized light along the $\Gamma \rightarrow$ X direction (same setup as in numerical simulations shown in Fig. 2d), fitted with the TCMT expression (equation (S20) in Supplementary Information) (black dashed lines). At each angle, the positions of the complex eigenvalues extracted experimentally are shown as open circles. **b**, Complex eigenvalues extracted experimentally (symbols), with comparison to numerical simulation results (dashed lines) for both the real part (left panel) and the imaginary part (right panel). Red squares and dashed lines are used for the band with zero radiation loss at the Γ point, blue circles and dashed lines for the band with finite radiation loss at the Γ point, and grey crosses and dashed lines for the third band decoupled from the previous two owing to symmetry. The orange shaded regions correspond to the inside of the ring. **c**, Positions of the eigenvalues (red and blue dashed lines) approach and become very close to each other (indicated by the two brown arrows), demonstrating near-EP features in different directions in the momentum space and the existence of an exceptional ring.

(non-resonant) and the resonant reflection processes including nearby resonances; the expression for reflectivity is given in Supplementary Information equation (S20), with the full derivation given in Supplementary Information section IX. Fitting the reflectivity curves with the TCMT expression gives us an accurate estimate of the matrix elements and the eigenvalues; this procedure is the same as our approach in ref. 27 except that here we additionally account for the coupling between resonances[28]. Figure 3a compares the fitted and the measured reflectivity curves at three representative angles (with more comparison in Supplementary Fig. 8a); the excellent agreement shows the validity of the TCMT model. Underneath the reflectivity curves, we show the complex eigenvalues. The difference between numerically calculated reflectivity (Fig. 2d) and experimental results (Fig. 3a) stems from the non-radiative decay channels in our system, mostly due to scattering loss from the surface roughness[24].

Repeating the fitting procedure for the reflectivity spectrum measured at different angles, we obtain the dispersion curves for all complex eigenvalues, which are plotted in Fig. 3b. Along both directions in k space ($\Gamma \rightarrow$ X and $\Gamma \rightarrow$ M), the two bands of interest (shown in blue and red) exhibit the EP behaviour predicted in equation (2): for $|\boldsymbol{k}| < k_c$ the real parts are degenerate and dispersionless; for $|\boldsymbol{k}| > k_c$ the imaginary parts are degenerate and dispersionless; for $|\boldsymbol{k}|$ in the vicinity of k_c branching features are observed in the real or imaginary part. In Fig. 3c, we plot the eigenvalues on the complex plane for both the $\Gamma \rightarrow$ X and $\Gamma \rightarrow$ M directions. We can see that in both directions, the two eigenvalues approach each other and become very close at a certain k point, which is a clear signature of the system being very close to an EP.

We have shown that non-Hermiticity arising from radiation can significantly alter fundamental properties of the system, including the band structures and the density of states; this effect becomes most prominent near EPs. The photonic crystal slab described here provides a simple-to-realize platform for studying the influence of EPs on light–matter interaction, such as for single particle detection[21] and modulation of quantum noise. The two-dimensional flat band can also provide a high density of states and therefore high Purcell factors. The strong dispersion of loss in the vicinity of the Γ point can improve the performance of large-area single-mode photonic crystal lasers[29]. The deformation into an exceptional ring is a general phenomenon that can also be achieved with material gain or loss and for Dirac points in other lattices[19,20]. Further studies could advance the understanding of the connection between the topological property of Dirac points[30] and that of EPs[25] in general non-Hermitian wave systems, and our method could go beyond photons to phonons, electrons and atoms.

Received 2 April; accepted 29 June 2015.
Published online 9 September 2015.

1. Castro Neto, A. H., Guinea, F., Peres, N. M. R., Novoselov, K. S. & Geim, A. K. The electronic properties of graphene. *Rev. Mod. Phys.* **81,** 109–162 (2009).
2. Rechtsman, M. C. *et al.* Strain-induced pseudomagnetic field and photonic landau levels in dielectric structures. *Nature Photon.* **7,** 153–158 (2013).
3. Tarruell, L., Greif, D., Uehlinger, T., Jotzu, G. & Esslinger, T. Creating, moving and merging Dirac points with a Fermi gas in a tunable honeycomb lattice. *Nature* **483,** 302–305 (2012).
4. Huang, X., Lai, Y., Hang, Z. H., Zheng, H. & Chan, C. Dirac cones induced by accidental degeneracy in photonic crystals and zero-refractive-index materials. *Nature Mater.* **10,** 582–586 (2011).
5. Moitra, P. *et al.* Realization of an all-dielectric zero-index optical metamaterial. *Nature Photon.* **7,** 791–795 (2013).
6. Moiseyev, N. *Non-Hermitian Quantum Mechanics* (Cambridge Univ. Press, 2011).
7. Rotter, I. A non-Hermitian Hamilton operator and the physics of open quantum systems. *J. Phys. A* **42,** 153001 (2009).
8. Bender, C. M. & Boettcher, S. Real spectra in non-Hermitian Hamiltonians having PT symmetry. *Phys. Rev. Lett.* **80,** 5243–5246 (1998).
9. Rüter, C. E. *et al.* Observation of parity–time symmetry in optics. *Nature Phys.* **6,** 192–195 (2010).

10. Chong, Y., Ge, L. & Stone, A. D. PT-symmetry breaking and laser-absorber modes in optical scattering systems. *Phys. Rev. Lett.* **106,** 093902 (2011).
11. Regensburger, A. *et al.* Parity-time synthetic photonic lattices. *Nature* **488,** 167–171 (2012).
12. Guo, A. *et al.* Observation of PT-symmetry breaking in complex optical potentials. *Phys. Rev. Lett.* **103,** 093902 (2009).
13. Lin, Z. *et al.* Unidirectional invisibility induced by PT-symmetric periodic structures. *Phys. Rev. Lett.* **106,** 213901 (2011).
14. Peng, B. *et al.* Parity–time-symmetric whispering-gallery microcavities. *Nature Phys.* **10,** 394–398 (2014).
15. Liertzer, M. *et al.* Pump-induced exceptional points in lasers. *Phys. Rev. Lett.* **108,** 173901 (2012).
16. Hodaei, H., Miri, M.-A., Heinrich, M., Christodoulides, D. N. & Khajavikhan, M. Parity-time–symmetric microring lasers. *Science* **346,** 975–978 (2014).
17. Feng, L., Wong, Z. J., Ma, R.-M., Wang, Y. & Zhang, X. Single-mode laser by parity-time symmetry breaking. *Science* **346,** 972–975 (2014).
18. Berry, M. Physics of nonhermitian degeneracies. *Czech. J. Phys.* **54,** 1039–1047 (2004).
19. Makris, K., El-Ganainy, R., Christodoulides, D. & Musslimani, Z. H. Beam dynamics in PT symmetric optical lattices. *Phys. Rev. Lett.* **100,** 103904 (2008).
20. Szameit, A., Rechtsman, M. C., Bahat-Treidel, O. & Segev, M. PT-symmetry in honeycomb photonic lattices. *Phys. Rev. A* **84,** 021806 (2011).
21. Cao, H. & Wiersig, J. Dielectric microcavities: model systems for wave chaos and non-Hermitian physics. *Rev. Mod. Phys.* **87,** 61–111 (2015).
22. Sakoda, K. Proof of the universality of mode symmetries in creating photonic Dirac cones. *Opt. Express* **20,** 25181–25194 (2012).
23. Chan, C., Hang, Z. H. & Huang, X. Dirac dispersion in two-dimensional photonic crystals. *Adv. Optoelectron.* **2012,** 313984 (2012).
24. Lee, J. *et al.* Observation and differentiation of unique high-*Q* optical resonances near zero wave vector in macroscopic photonic crystal slabs. *Phys. Rev. Lett.* **109,** 067401 (2012).
25. Dembowski, C. *et al.* Experimental observation of the topological structure of exceptional points. *Phys. Rev. Lett.* **86,** 787–790 (2001).
26. Hsu, C. W., DeLacy, B. G., Johnson, S. G., Joannopoulos, J. D. & Soljacic, M. Theoretical criteria for scattering dark states in nanostructured particles. *Nano Lett.* **14,** 2783–2788 (2014).
27. Hsu, C. W. *et al.* Observation of trapped light within the radiation continuum. *Nature* **499,** 188–191 (2013).
28. Suh, W., Wang, Z. & Fan, S. Temporal coupled-mode theory and the presence of non-orthogonal modes in lossless multimode cavities. *IEEE J. Quantum Electron.* **40,** 1511–1518 (2004).
29. Chua, S.-L., Lu, L., Bravo-Abad, J., Joannopoulos, J. D. & Soljačić, M. Larger-area single-mode photonic crystal surface-emitting lasers enabled by an accidental Dirac point. *Opt. Lett.* **39,** 2072–2075 (2014).
30. Lu, L., Joannopoulos, J. D. & Soljacic, M. Topological photonics. *Nature Photon.* **8,** 821–829 (2014).

Supplementary Information is available in the online version of the paper.

Acknowledgements We thank T. Savas for fabrication of the samples, and F. Wang, Y. Yang, N. Rivera, S. Skirlo, O. Miller and S. G. Johnson for discussions. This work was partly supported by the Army Research Office through the Institute for Soldier Nanotechnologies under contract nos W911NF-07-D0004 and W911NF-13-D-0001. B.Z., L.L. and M.S. were partly supported by S3TEC, an Energy Frontier Research Center funded by the US Department of Energy under grant no. DE-SC0001299. L.L. was supported in part by the Materials Research Science and Engineering Center of the National Science Foundation (award no. DMR-1419807). I.K. was supported in part by Marie Curie grant no. 328853-MC-BSiCS.

Author Contributions All authors discussed the results and made critical contributions to the work.

Author Information Reprints and permissions information is available at www.nature.com/reprints. The authors declare no competing financial interests. Readers are welcome to comment on the online version of the paper. Correspondence and requests for materials should be addressed to B.Z. (bozhen@mit.edu) and C.W.H. (chiawei.hsu@yale.edu).

doi:10.1038/nature14889

Section I. Effective Hamiltonian of accidental Dirac points in Hermitian systems

Here we consider the Hermitian system of a 2D square-lattice PhC tuned to accidental degeneracy between a quadrupole mode and two degenerate dipole modes at the Brillouin zone center (Γ point). Near Γ point where the in-plane wavevectors k_x and k_y are small, the effective Hamiltonian given by first-order degenerate perturbation theory is [1]

$$H_{\text{eff}}^{\text{2D}} = \begin{pmatrix} \omega_0 & v_g k_x & v_g k_y \\ v_g k_x & \omega_0 & 0 \\ v_g k_y & 0 & \omega_0 \end{pmatrix}, \tag{S.1}$$

which can be transformed to

$$U H_{\text{eff}}^{\text{2D}} U^{-1} = \begin{pmatrix} \omega_0 & v_g|\mathbf{k}| & 0 \\ v_g|\mathbf{k}| & \omega_0 & 0 \\ 0 & 0 & \omega_0 \end{pmatrix} \tag{S.2}$$

with the orthogonal rotation matrix

$$U = \begin{pmatrix} 1 & 0 & 0 \\ 0 & \cos\theta & \sin\theta \\ 0 & -\sin\theta & \cos\theta \end{pmatrix} \tag{S.3}$$

where $\cos\theta = k_x/|\mathbf{k}|$, $\sin\theta = k_y/|\mathbf{k}|$, and $|\mathbf{k}| = \sqrt{k_x^2 + k_y^2}$. After transformation, the 3×3 matrix becomes two isolated blocks: the upper 2×2 block gives the conical Dirac dispersion ($\omega = \omega_0 \pm v_g|\mathbf{k}|$), while the lower block is the intersecting flat band ($\omega = \omega_0$).

Section II. Effective non-Hermitian Hamiltonian of the exceptional ring

For a 3D PhC slab with finite thickness, the two dipole modes become resonances with finite lifetime due to their radiation, with eigenvalues becoming complex ($\omega_0 - i\gamma_{\text{d}}$). With C_4 rotational symmetry, these two dipole modes are related by a 90° rotation and therefore share the same complex eigenvalue. Meanwhile, the quadrupole mode does not couple to radiation at the Γ point due to symmetry mismatch [2], and to leading order its eigenvalue remains at ω_0. The effective non-Hermitian Hamiltonian of the 3D PhC slab thus becomes

$$H_{\text{eff}}^{\text{3D}} = \begin{pmatrix} \omega_0 & v_g k_x & v_g k_y \\ v_g k_x & \omega_0 - i\gamma_{\text{d}} & 0 \\ v_g k_y & 0 & \omega_0 - i\gamma_{\text{d}} \end{pmatrix}, \tag{S.4}$$

which transforms to

$$U H_{\text{eff}}^{\text{3D}} U^{-1} = \begin{pmatrix} \omega_0 & v_g|\mathbf{k}| & 0 \\ v_g|\mathbf{k}| & \omega_0 - i\gamma_{\text{d}} & 0 \\ 0 & 0 & \omega_0 - i\gamma_{\text{d}} \end{pmatrix} \tag{S.5}$$

with the same matrix U as in equation (S.3). The upper 2×2 block is the H_{eff} in equation (1) of the main text that gives rise to an exceptional ring, while the lower block is the flat band.

Section III, Eigenfunctions in Hermitian and non-Hermitian systems

In this section, we show the numerically calculated eigenfunctions in the Hermitian PhC and the non-Hermitian PhC slab, and compare them to the analytical predictions from first-order perturbation theory.

According to equation S.1, the eigenfunctions of the Hermitian PhC along the k_x axis are $\Psi_1 \pm \Psi_2$ with eigenvalues $\omega_0 \pm v_g k_x$. Fig. S1a shows that the numerical results agree with this prediction. These two eigenfunctions are orthogonal to each other, as expected for Hermitian systems.

In comparison, for the non-Hermitian PhC slab, equation S.4 predicts the two eigenfunctions to merge into one, $\Psi_1 - i\,\Psi_2$, at the exceptional point (EP). This prediction also agrees with our numerical results, shown in Fig. S1b. Both eigenfunctions become very close to the analytical prediction of $\Psi_1 - i\,\Psi_2$. Furthermore, this coalesced eigenfunction is self-orthogonal under the unconjugated product. Such coalescence of eigenfunctions can never happen in Hermitian systems and highlights the effect of non-Hermiticity.

Section IV, Existence of exceptional points along every direction in momentum space

In this section, we demonstrate that EPs exist in all directions in the k space, not only for a simplified Hamiltonian (equation (1)), but also for realistic structures. To prove their existence, we use the unique topological property of EPs: when the system evolves adiabatically in the parameter space around an EP, the eigenvalues will switch their positions at the end of the loop [3,4]. In our system, the parameter space in which we choose to evolve the eigenfunctions is three-dimensional, consisting of the two in-plane wavevectors (k_x, k_y) and the radius of the air holes r, as shown in Fig. S3a. Here, r can also be other parameters, like the refractive index of the PhC slab (n), the periodicity of the square lattice (a), or the thickness of the slab (h). For simplicity of this demonstration, we choose r as the varying parameter while keeping all other parameters (n, a, and h) fixed throughout.

First, we compare the evolution of the eigenvalues when the system parameters follow (1) a loop that does not enclose an EP, and (2) one that encloses an EP. Following the loop $A \rightarrow B \rightarrow C \rightarrow D \rightarrow A$ in Fig. S3a,b that does not enclose an EP (point $\mathrm{E_P}$), we see that the complex eigenvalues come back to themselves at the end of the loop (Fig. S3c where the red dot and the blue dot return to their initial positions at the end of the loop). However, following the loop $A' \rightarrow B' \rightarrow C' \rightarrow D' \rightarrow A'$ in Fig. S3d, which encloses an EP (point $\mathrm{E_P}$), we see that the complex eigenvalues switch their positions in the complex plane (Fig. S3f where the red dot and the blue dot switch their positions). This switching of the eigenvalues shows the existence of an EP along the Γ to X direction, at some particular value of k_x and some particular value of radius r. This shows the existence of the EP without having to locate the exact parameters of k_x and r at which the EP occurs.

Similarly, we can evolve the parameters along any direction $\theta = \tan(k_y/k_x)$ in the k space and check whether an EP exists along this direction or not. As two examples, we show the evolution of the complex eigenvalues when we evolve the parameters along the $\theta = \pi/8$ direction following the loop $A'' \rightarrow B'' \rightarrow C'' \rightarrow D'' \rightarrow A''$ and along the $\theta = \pi/4$ direction following

the loop $A''' \rightarrow B''' \rightarrow C''' \rightarrow D''' \rightarrow A'''$ in Fig. S3g,h. In both cases, we observe the switching of the eigenvalues, showing the existence of an EP along these two directions. The same should hold for every direction in k space.

The above calculations show that for every direction θ we examined in the k space, there is always a particular combination of k_c and r_c, which supports an EP. However, we note that in general, different directions can have different k_c and different r_c, so the exceptional ring for the realistic PhC slab structure is parameterized by $k_c(\theta)$ and $r_c(\theta)$. This angular variation of $k_c(\theta)$ and $r_c(\theta)$ can be described by introducing higher order corrections in the effective Hamiltonian, which we examine in the next section.

Section V, Generalization of the effective Hamiltonian

Here, we generalize the effective Hamiltonian in equations (1) and (S.5). First, the radiation of the quadrapole mode is zero only at the Γ point; away from the Γ point, the quadrapole mode has a $\vec{k}$-dependent radiation that is small but non-zero, which we denote with γ_{q}. Second, we consider possible deviation from accidental degeneracy in the Hermitian part, with a frequency walk-off δ. With these two additional ingredients, the effective Hamiltonian becomes

$$\begin{pmatrix} \omega_0+\delta & v_g k \\ v_g k & \omega_0 \end{pmatrix} - i \begin{pmatrix} \gamma_{\mathrm{q}} & \sqrt{\gamma_{\mathrm{q}}\gamma_{\mathrm{d}}} \\ \sqrt{\gamma_{\mathrm{q}}\gamma_{\mathrm{d}}} & \gamma_{\mathrm{d}} \end{pmatrix}, \tag{S.6}$$

with complex eigenvalues of

$$\omega_{\pm} = \omega_0 + \frac{\delta}{2} - i\frac{\gamma_{\mathrm{q}}+\gamma_{\mathrm{d}}}{2} \pm \sqrt{\left(v_g k - i\sqrt{\gamma_{\mathrm{q}}\gamma_{\mathrm{d}}}\right)^2 - \left(\frac{\gamma_{\mathrm{d}}-\gamma_{\mathrm{q}}}{2} - i\frac{\delta}{2}\right)^2}, \tag{S.7}$$

which are generalized forms of equations (1) and (2), respectively. We note that the off-diagonal term $\sqrt{\gamma_{\mathrm{q}}\gamma_{\mathrm{d}}}$ in equation (S.6) is required by energy conservation and time-reversal symmetry [5], as we will discuss more in the last section. Equation (S.7) shows that EP occurs when the two conditions

$$\begin{cases} k = (\gamma_{\mathrm{d}} - \gamma_{\mathrm{q}})/(2v_g) \approx \gamma_{\mathrm{d}}/2v_g, \\ \delta = 2\sqrt{\gamma_{\mathrm{d}}\gamma_{\mathrm{q}}}, \end{cases} \tag{S.8}$$

are satisfied. In the region of momentum space of interest, γ_{q} is much smaller than γ_0 (this can be seen, for example, from the imaginary parts of Fig. S2a,c), so the first condition becomes $k_{\mathrm{c}} \approx \gamma_{\mathrm{d}}/2v_g$, same as in the simplified model. For a given direction θ in the k space (as discussed in the previous section), we can vary the magnitude k and the radius r to find the $k_c(\theta)$ and $r_c(\theta)$ where these two conditions are met simultaneously.

We can now analyze the angular dependence of $k_c(\theta)$ and $r_c(\theta)$ without having to find their exact values. The first condition of equation (S.8) says that the angular dependence of $k_c(\theta)$ comes from γ_{d} and v_g; in the PhC slab structure here, we find that γ_{d} varies by about 20% as the angle $\theta = \tan(k_y/k_x)$ is varied, while v_g remains almost the same; therefore, $k_c(\theta)$ potentially varies by around 10% along the exceptional ring. For the second condition of equation (S.8), we have $\gamma_{\mathrm{d}} \approx 5\times10^{-3}\omega_0$ and $\gamma_{\mathrm{q}} \approx 5\times10^{-5}\omega_0$ for our PhC slab structure, so

$\delta_c = 2\sqrt{\gamma_d \gamma_q} \approx 1 \times 10^{-3}\omega_0$. Again, γ_d and γ_q vary by about 20% as the angle θ is changed, so δ_c can change by around $2 \times 10^{-4}\omega_0$. Empirically, we find that a change of δ by $2 \times 10^{-4}\omega_0$ corresponds to a change in the radius r of around 0.06 nm, which is the estimated range of variation for $r_c(\theta)$ of all $\theta \in [0, 2\pi)$. This angular variation is much smaller than our structure can resolve in practice, since the radii of different holes within one fabricated PhC slab will already differ by more than 0.06 nm. So, in practice a given fabricated structure can be close to EP along all different directions θ, but is unlikely to be an exact EP for any direction.

Section VI, Sample fabrication and experimental details

The Si_3N_4 layer was grown with the low-pressure chemical vapor deposition method on a 6μm-thick cladding of SiO_2 on the backbone of a silicon wafer (LioniX). Before exposure, the wafer was coated with a layer of polymer as anti-reflection coating, a thin layer of SiO_2 as an intermediate layer for etching, and a layer of negative photoresist for exposure. The square lattice pattern was created with Mach−Zehnder interference lithography using a 325-nm He/Cd laser. The angle between the two arms of the laser beam was chosen for a periodicity of 336 nm. After exposures, the pattern in the photoresist was transferred to Si_3N_4 by reactive-ion etching.

The source was a supercontinuum laser from NKT Photonics (SuperKCompact). A polarizer selected s- or p-polarized light. The sample was immersed in a colorless liquid with tunable refractive indices (Cargille Labs). The sample was mounted on two perpendicular motorized rotation stages (Newport): one to orient the PhC to the Γ-X or Γ-M direction, and the other to determine the incident angle θ. The reflectivity spectra were measured with a spectrometer with spectral resolution of 0.02 nm (HR4000; Ocean Optics).

Section VII, Model of reflection from two resonances

In Section IX, we will derive the temporal-coupled coupled theory (TCMT) [5–10] equations describing the full experimental system. Here, we first consider a simpler scenario to illustrate the qualitative features of the reflectivity spectrum. Consider two resonances in a photonic crystal slab, governed by the Hamiltonian in equation (3) of the main text,

$$H = \begin{pmatrix} \omega_1 & \kappa \\ \kappa & \omega_2 \end{pmatrix} - i \begin{pmatrix} \gamma_1 & \gamma_{12} \\ \gamma_{12} & \gamma_2 \end{pmatrix}, \tag{S.9}$$

where the first term is the Hermitian part describing a lossless system, and the second term is the anti-Hermitian part describing radiation of the two resonances. We ignore non-radiative loss here for simplicity. Also, we ignore the direct Fresnel reflection between the dielectric layers. We consider the photonic crystal slab to be mirror symmetric in z direction, with the two resonances having the same mirror symmetry in z. This simple system describes the basic elements of resonant reflection. TCMT predicts the reflectivity to be (see Section IX for the full details)

$$R(\omega) = \frac{1}{1 + f^2(\omega)}, \quad f(\omega) = \frac{(\omega - \omega_1)(\omega - \omega_2) - \kappa^2}{\gamma_1(\omega - \omega_2) + \gamma_2(\omega - \omega_1) + 2\gamma_{12}\kappa} \tag{S.10}$$

with the transmission being $T(\omega) = 1 - R(\omega)$ since there is no non-radiative loss. We immediately see that the reflectivity reaches its maximal value of 1 when the numerator of $f(\omega)$ vanishes, which happens at two frequencies $\omega = \Omega_{1,2}$ with

$$\Omega_{1,2} = \frac{1}{2}\left[\omega_1 + \omega_2 \pm \sqrt{(\omega_1 - \omega_2)^2 + 4\kappa^2}\right] \tag{S.11}$$

being the eigenvalues for the Hermitian part of the Hamiltonian. Note that the anti-Hermitian part determines the linewidth but has no effect on the location of the reflectivity peaks. This is the first main conclusion of this section.

Secondly, we also observe that the reflectivity reaches its minimal value of 0 when the denominator of $f(\omega)$ vanishes, which happens at one frequency $\omega = (\gamma_1\omega_2 + \gamma_2\omega_1 - 2\gamma_{12}\kappa)/(\gamma_1 + \gamma_2)$ that is in between Ω_1 and Ω_2. This is called coupled-resonator-induced transparency (CRIT) [11, 12].

We emphasize that the reflectivity peaks, following eigenvalues of the Hermitian part of the Hamiltonian, are different from the real part of the complex eigenvalues of the Hamiltonian H. Consider a simple example with $\kappa = 0$ (so that $\Omega_{1,2} = \omega_{1,2}$), $\Omega_{1,2} = \omega_0 \pm b$, and $\gamma_1 = \gamma_2 = \gamma_{12} = b$. The reflection peaks at $\Omega_{1,2} = \omega_0 \pm b$, while the two complex eigenvalues are degenerate at $\omega_+ = \omega_- = \omega_0 - ib$, whose real part is in the middle of the two reflection peaks. This explains the reflectivity from the PhC slabs at 0.3° shown in Fig. 2d and Fig. 3a, where the degenerate complex eigenvalues of the system are in between the two reflection peaks.

In Fig. S6, we use some examples to illustrate the difference between the reflectivity peaks and the real part of the complex eigenvalues. Fig. S6a shows the case when there is only one resonance with complex eigenvalue $\omega_0 - i\gamma$; in this case, the reflection peak (red arrow) is at the same position as the real part of the complex eigenvalue. In contrast, Fig. S6b shows the case when there are two resonances [equation (S.10)] with $\kappa = 0$ and $\Omega_{1,2}$ fixed at $\omega_0 \pm b$; as we vary $\gamma_{1,2}$, the complex eigenvalues (circles) vary accordingly, whereas the reflectivity peaks (red arrows) always show up at $\Omega_{1,2}$.

Section VIII, Effects of material loss and gain

The conclusion that reflectivity peaks at the eigenfrequencies $\Omega_{1,2}$ of the Hermitian part is valid when radiation is the only source of loss and when there is no gain in the system. It no longer holds when substantial material loss and/or gain is introduced, as we show in this section.

To account for material loss and gain, we extend the Hamiltonian in Section VII to

$$H = \begin{pmatrix} \omega_1 & \kappa \\ \kappa & \omega_2 \end{pmatrix} - \underbrace{i\begin{pmatrix} \gamma_1 & \gamma_{12} \\ \gamma_{12} & \gamma_2 \end{pmatrix}}_{\text{Radiation loss}} - \underbrace{i\begin{pmatrix} \eta_1 & 0 \\ 0 & \eta_2 \end{pmatrix}}_{\text{Material loss/gain}} \tag{S.12}$$

with positive (negative) values of $\eta_{1,2}$ describing material loss (gain). Same derivation using

TCMT yields reflection and transmission as

$$R(\omega) = |g(\omega)|^2, \quad T(\omega) = |1 + g(\omega)|^2$$
$$g(\omega) = i\frac{\gamma_1(\omega_2 - i\eta_2 - \omega) + \gamma_2(\omega_1 - i\eta_1 - \omega) - 2\gamma_{12}\kappa}{(\omega_1 - i\gamma_1 - i\eta_1 - \omega)(\omega_2 - i\gamma_2 - i\eta_2 - \omega) - (\kappa - i\gamma_{12})^2}. \tag{S.13}$$

When $\eta_{1,2}$ is small, the expression reduces back to equation (S.10). When $\eta_{1,2}$ is substantial, neither the reflectivity peaks nor the transmission dips follow the eigenvalues $\Omega_{1,2}$.

To illustrate this point, we consider a system tuned to accidental degeneracy ($\omega_1 = \omega_2 \equiv \omega_0$) with only one resonance radiating ($\gamma_1 = 1$, $\gamma_2 = \gamma_{12} = 0$) and with equal gain/loss for the two resonances ($\eta_1 = \eta_2 \equiv \eta_0$). This system has linear Dirac dispersion $\Omega_{1,2} = \omega_0 \pm \kappa$ for the eigenfrequency of the Hermitian part, while the complex eigenvalues exhibit an exceptional point at $\kappa = 1/2$. In Fig. S7, we plot the reflection and transmission spectrum for a system with substantial non-radiative loss ($\eta_0 = 0.45$, Fig. S7a), a purely passive system ($\eta_0 = 0$, Fig. S7b), and a system with substantial gain ($\eta_0 = -0.25$, Fig. S7c). On top of the plots, we indicate the reflection peaks (blue solid lines) and transmission dips (red solid lines), as well as the eigenfrequency of the Hermitian part (green dashed lines) and the real part of the eigenvalues (green solid lines). As can be seen, in the passive case the reflection peaks and transmission dips follow the linear dispersion of $\Omega_{1,2}$, whereas in the cases with substantial non-radiative loss or material gain, the reflection peaks and transmission dips show branching behavior instead.

Section IX, Full derivation using temporal coupled-mode theory (TCMT)

Here, we provide the derivation of reflectivity using temporal coupled-mode theory (TCMT) [5–10] in a more general setup than the previous two sections. We will account for the direct (non-resonant) reflection process in between layers of dielectric, include arbitrary number of n resonances (as there are other nearby resonances that modify the spectrum) with arbitrary symmetries, and account for the non-radiative loss. We use the resulting expression to fit the experimentally measured reflection data and extract the Hamiltonian matrix elements and eigenvalues.

The time evolution of these n resonances, whose complex amplitudes are denoted by an $n \times 1$ column vector A, is described by the Hamiltonian H and a driving term,

$$\frac{dA}{dt} = -iHA + K^{\mathrm{T}} s_+, \tag{S.14}$$

where the Hamiltonian is an $n \times n$ non-Hermitian matrix

$$H = \Omega - i\Gamma - i\gamma_{\mathrm{nr}}, \tag{S.15}$$

with Ω denoting its Hermitian part that describes a lossless system, $-i\Gamma$ denoting its anti-Hermitian part from radiation loss, and $-i\gamma_{\mathrm{nr}}$ its anti-Hermitian part from non-radiative decays. The non-radiative decay includes both material absorption and scattering from surface roughness (in our system, surface roughness is the primary contribution [2]), and here we consider it to be the same for all resonances, so γ_{nr} is a real number instead of a matrix.

Reflectivity measurements couple the n resonances to the incoming and outgoing planewaves, whose complex amplitudes we denote by two 2×1 column vectors, s_+ and s_-. The direct reflection and transmission of the planewaves through the slab (in the absence of resonances) are described by a 2×2 complex symmetric matrix C, and

$$s_- = Cs_+ + DA, \tag{S.16}$$

where D and K in equation (S.14) are $2 \times n$ complex matrices denoting coupling between the resonances and the planewaves. We approximate the direct scattering matrix C by that of a homogeneous slab whose permittivity is equal to the spatial average of the PhC slab [8–10]. Lastly, outgoing planewaves into the silica substrate are reflected at the silica-silicon interface, so

$$s_{2+} = e^{2i\beta h_s} r_{23} s_{2-}, \tag{S.17}$$

where h_s is the thickness of the silica substrate with refractive index $n_s = 1.46$, $\beta = \sqrt{\frac{n_s^2\omega^2}{c^2} - |\mathbf{k}_{\|}|^2}$ is the propagation constant in silica, and r_{23} is the Fresnel reflection coefficient between silica and the underlying silicon. The formalism described above is the same as Ref [9] except that here we account for the coupling between the n resonances (off-diagonal terms of H).

For steady state with $e^{-i\omega t}$ time dependence, we solve for vector A from equation (S.14) to get the scattering matrix of the whole system that includes both direct and resonant processes,

$$s_- = (C + C_{\text{res}})s_+, \tag{S.18}$$

where the effect of the n resonances is captured in a 2×2 matrix

$$C_{\text{res}} = iD(\omega - H)^{-1}K^{\text{T}}. \tag{S.19}$$

We can solve equation (S.17) and equation (S.18) to obtain the reflectivity

$$R(\omega) = \left| \frac{s_{1-}}{s_{1+}} \right|^2. \tag{S.20}$$

In this expression, the only unknown is C_{res}. Therefore, by comparing the experimentally measured reflectivity spectrum and the one given by TCMT in equation (S.20), we can extract the unknown parameters in the resonant scattering matrix C_{res} and obtain the eigenvalues of the Hamiltonian H.

The remaining task is to write C_{res} using as few unknowns as possible so that the eigenvalues of H can be extracted unambiguously. In equation (S.19), there are a large number of unknowns in the matrix elements of H, D, and K, but there is much redundancy because the matrix elements are not independent variables and because C_{res} is independent of the basis choice. Below, we show that we can express C_{res} with only $2n + 1$ unknown real numbers, and these $2n + 1$ real numbers are enough to determine the n complex eigenvalues of H.

First, we normalize the amplitudes of A and $s_\pm$ such that their magnitudes squared are the energy of the resonances per unit cell and the power of the incoming/outgoing planewaves per

unit cell, respectively. Then, energy conservation, time-reversal symmetry, and C_2 rotational symmetry of the PhC slab [5, 13] require the direct scattering matrix to satisfy $C^\dagger = C^* = C^{-1}$ and the coupling matrices to satisfy $D^\dagger D = 2\Gamma$, $K = D$, and $CD^* = -D$. It follows that the matrix Γ is real and symmetric. Next, using the Woodbury matrix identity and these constraints, we can rewrite equation (S.19) as

$$C_{\text{res}} = -2W\left(2 + W\right)^{-1} C, \tag{S.21}$$

where $W \equiv iD(\omega - \Omega + i\gamma_0)^{-1}D^\dagger$ is a 2-by-2 matrix.

We note that the matrix W, and therefore the matrix C_{res}, is invariant under a change of basis for the resonances through any orthogonal matrix U (where Ω is transformed to $U\Omega U^{-1}$, and D is transformed to DU^{-1}). The eigenvalues of H is also invariant under a change of basis. Therefore, we are free to choose any basis. We kept the basis choice general in the two-resonance system described in the previous two sections, but here for the purpose of fitting, we need as few unknowns as possible, and it is most convenient to choose the basis where Ω is diagonal. So we let $\Omega_{ij} = \Omega_j \delta_{ij}$, with $\{\Omega_j\}_{j=1}^n$ being the eigenvalues of Ω.

To proceed further, we note that the PhC slab sits on a silica substrate with $n_{\text{s}} = 1.46$ and is immersed in a liquid with $n = 1.48$, so the structure is nearly symmetric in the z direction. The mirror symmetry requires the coupling to the two sides to be symmetric or anti-symmetric [7],

$$\frac{D_{1j}}{D_{2j}} \equiv \sigma_j = \pm 1, \quad j = 1, \ldots, n, \tag{S.22}$$

where $\sigma_j = 1$ for TE-like resonances and $\sigma_j = -1$ for TM-like resonances, in the convention where (E_x, E_y) determines the phase of A_j and $s_\pm$. Then, the diagonal elements of Γ are related to D by $\Gamma_{jj} \equiv \gamma_j = |D_{1j}|^2$, and in this basis we have

$$W = \sum_{j=1}^{n} \frac{i\gamma_j}{\omega - \Omega_j + i\gamma_{\text{nr}}} \begin{pmatrix} 1 & \sigma_j \\ \sigma_j & 1 \end{pmatrix}. \tag{S.23}$$

This completes our derivation. Equations (S.21) and (S.23) provide an expression for C_{res} that depends only on $2n + 1$ unknown non-negative real numbers: the n eigenvalues $\{\Omega_j\}_{j=1}^n$ of the Hermitian matrix Ω, the n diagonal elements $\{\gamma_j\}_{j=1}^n$ of the real-symmetric radiation matrix Γ in the basis where Ω is diagonal, and the non-radiative decay rate γ_{nr}.

At each angle and each polarization, we fit the experimentally measured reflectivity spectrum to the TCMT expression equation (S.20) to determine these $2n + 1$ unknown parameters. Fig. 3a and Fig. S8a show the comparison between the experimental reflectivity spectrum and the fitted TCMT reflectivity spectrum at some representative angles. The near-perfect agreement between the two demonstrates the validity of the TCMT model.

To obtain the eigenvalues of the Hamiltonian H, we also need to know the off-diagonal elements of Γ. From $D^\dagger D = 2\Gamma$ and $D_{1j}/D_{2j} = \sigma_j$, we see that $\Gamma_{ij} = 0$ when resonance i and resonance j have different symmetries in z (*i.e.* when $\sigma_i \sigma_j \neq 1$), and that $\Gamma_{ij} = \pm\sqrt{\gamma_i \gamma_j}$ when

$\sigma_i\sigma_j = 1$. In the latter case, the sign of Γ_{ij} depends on the choice of basis; the eigenvalues of H are independent of the basis choice, so to calculate the eigenvalues of H, we can simply take the positive roots of all of the non-zero off-diagonal elements of Γ.

We note that the model Hamiltonians introduced previously, such as equation (1) in the main text and equation (S.6) above, are all special cases of the general Hamiltonian in equation (S.15) that we consider in the TCMT formalism in this section. The TCMT formalism in this section does not make assumptions on the particular forms of the matrix elements (aside from basic principles such as energy conservation and time-reversal symmetry), so it can be used as an unbiased method for analyzing the experimental data.

References

[1] Sakoda, K. Proof of the universality of mode symmetries in creating photonic dirac cones. *Opt. Express* **20**, 25181–25194 (2012).

[2] Lee, J. *et al.* Observation and differentiation of unique high-Q optical resonances near zero wave vector in macroscopic photonic crystal slabs. *Phys. Rev. Lett.* **109**, 067401 (2012).

[3] Rotter, I. A non-Hermitian Hamilton operator and the physics of open quantum systems. *J. Phys. A* **42**, 153001 (2009).

[4] Dembowski, C. *et al.* Experimental observation of the topological structure of exceptional points. *Phys. Rev. Lett.* **86**, 787–790 (2001).

[5] Suh, W., Wang, Z. & Fan, S. Temporal coupled-mode theory and the presence of non-orthogonal modes in lossless multimode cavities. *IEEE J. Quantum Electron.* **40**, 1511–1518 (2004).

[6] Haus, H. A. *Waves and Fields in Optoelectronics* (Prentice-Hall, Englewood Cliffs, NJ, 1984).

[7] Joannopoulos, J. D., Johnson, S. G., Winn, J. N. & Meade, R. D. *Photonic Crystals: Molding the Flow of Light* (Princeton University Press, 2008), 2 edn.

[8] Fan, S. & Joannopoulos, J. D. Analysis of guided resonances in photonic crystal slabs. *Phys. Rev. B* **65**, 235112 (2002).

[9] Fan, S., Suh, W. & Joannopoulos, J. D. Temporal coupled-mode theory for the Fano resonance in optical resonators. *J. Opt. Soc. Am. A* **20**, 569–572 (2003).

[10] Hsu, C. W. *et al.* Observation of trapped light within the radiation continuum. *Nature* **499**, 188–191 (2013).

[11] Miroshnichenko, A. E., Flach, S. & Kivshar, Y. S. Fano resonances in nanoscale structures. *Rev. Mod. Phys.* **82**, 2257 (2010).

[12] Hsu, C. W., DeLacy, B. G., Johnson, S. G., Joannopoulos, J. D. & Soljacic, M. Theoretical criteria for scattering dark states in nanostructured particles. *Nano Lett.* **14**, 2783–2788 (2014).

[13] Hsu, C. W. *et al.* Bloch surface eigenstates within the radiation continuum. *Light: Science & Applications* **2**, e84 (2013).

SUPPLEMENTARY FIGURES

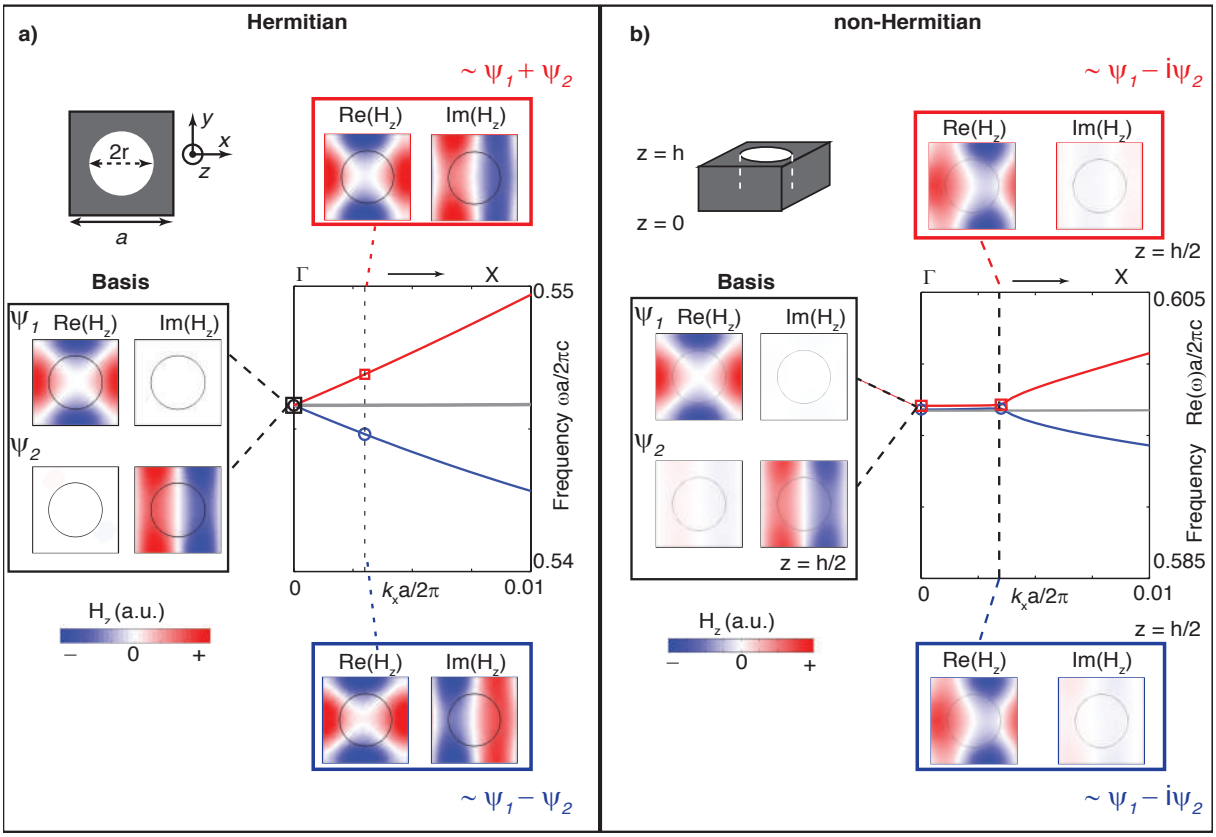

Supplementary Figure 1: **Eigenfunctions in the Hermitian PhC and the non-Hermitian PhC slab. a,** Numerically calculated band structure and eigenfunctions for the Hermitian 2D PhC. The basis eigenfunctions at the Γ point (Ψ_1 and Ψ_2) are shown in the black box. The eigenfunctions away from Γ point (at $k_x a/2\pi = 0.0035$) are shown in the red and blue boxes, agreeing well with the analytical prediction of $\Psi_1 \pm \Psi_2$. **b,** Corresponding results for the non-Hermitian PhC slab, showing the basis eigenfunctions at the Γ point (black box) and the two eigenfunctions near the exceptional point ($k_x a/2\pi = 0.0035$, red and blue boxes). The two eigenfunction near EP almost coalesce and both agree with the analytical prediction of $\Psi_1 - i\,\Psi_2$.

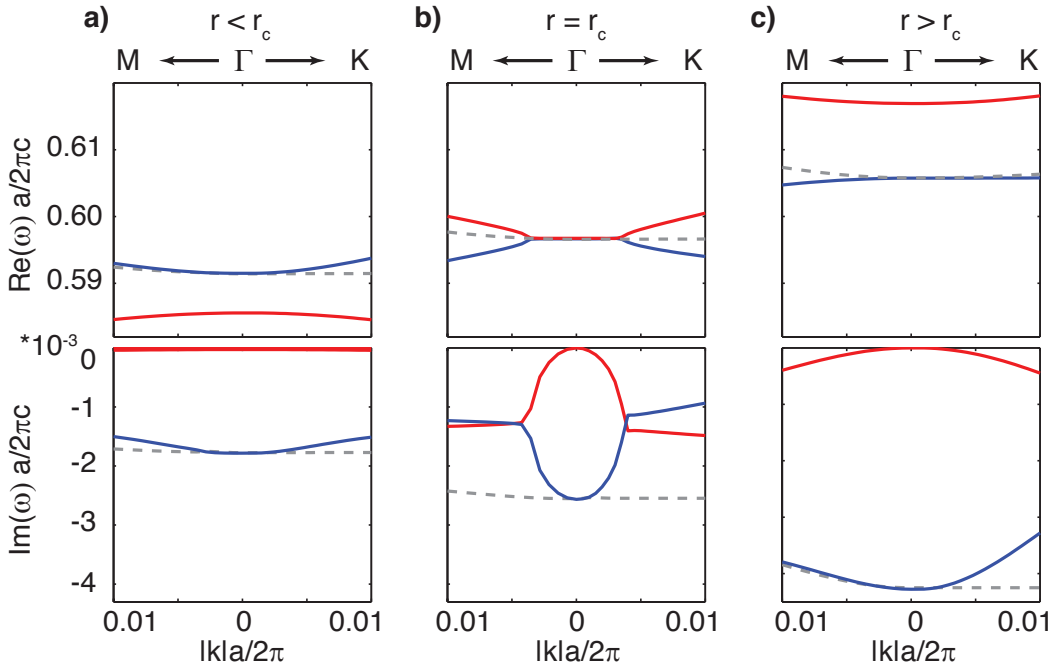

Supplementary Figure 2: **Simulation results of the complex eigenvalues of the PhC slabs with and without accidental degeneracy.** The real (upper panels) and imaginary (lower panels) parts of the complex eigenvalues are shown for structures with (**b**) and without (**a, c**) accidental degeneracy. The bands with quadrapole modes in the middle of the Brillouin zone are shown in red solid lines, while the bands with the dipole mode are shown in blue solid lines and gray dashed lines. The bands shown in red and blue solid lines couple to each other, while the band in gray dashed lines is decoupled from the other two due to symmetry. When accidental degeneracy happens (at $r = r_c$ as shown in **b**), the characteristic branching features are observed, demonstrating the existence of EPs. When the accidental degeneracy is lifted, the quadrupole band splits from the dipole bands from different directions: from the bottom when radius of the holes is too small ($r < r_c$ as shown in **a**), or from the top when the radius is too big ($r > r_c$ as shown in **c**).

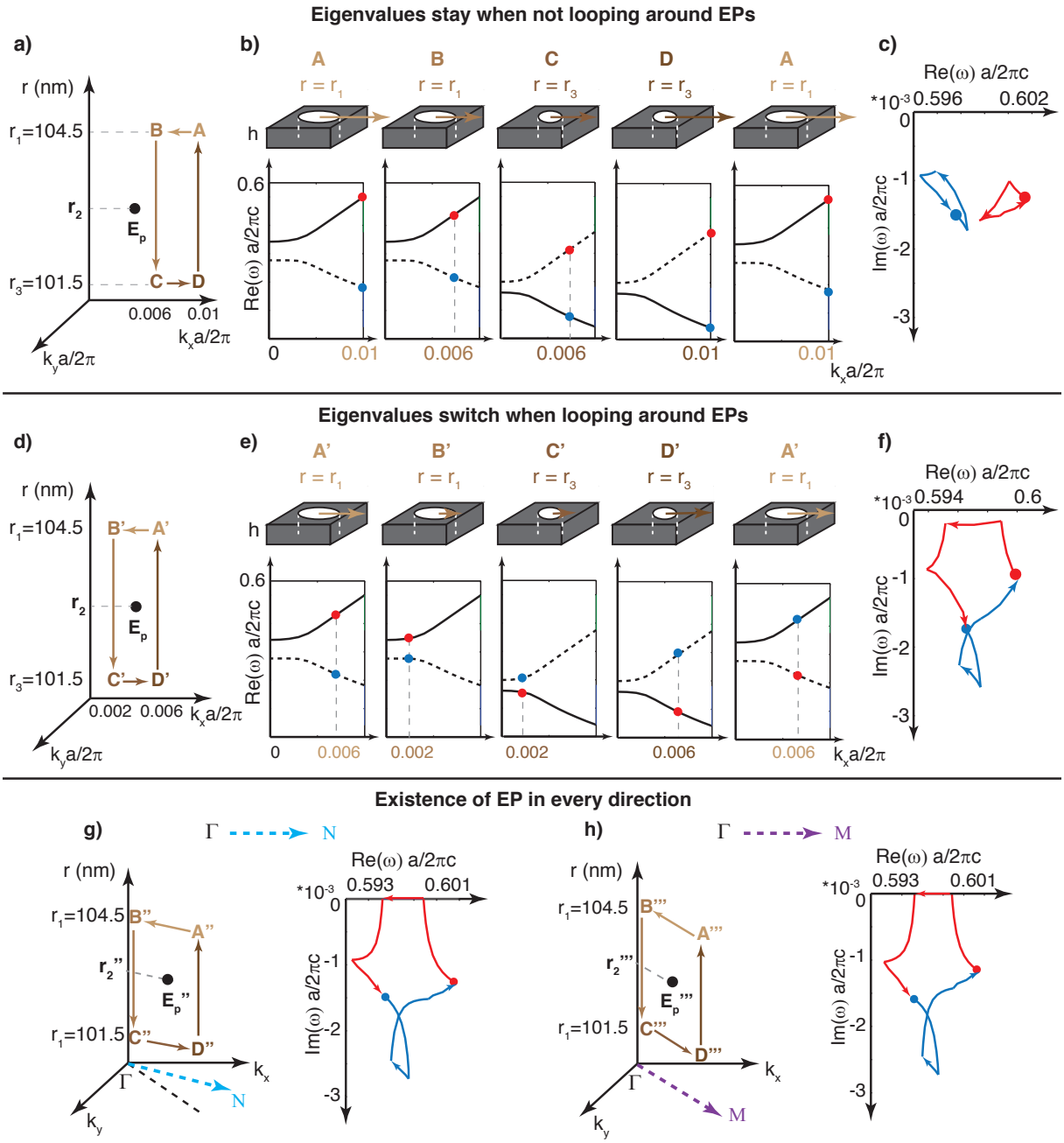

Supplementary Figure 3: **Existence of EP along every direction in the momentum space for the realistic PhC slab structure. a**, A loop is created in the parameter space of the structure $(A \rightarrow B \rightarrow C \rightarrow D \rightarrow A)$, which does not enclose the EP of the system (point $\mathrm{E_p}$). Here, r is the radius of the air holes, and $k_{x,y}$ are the in-plane wavevectors. **b**, For each point along the loop, we numerically calculate the eigenvalues of the PhC slab with the corresponding hole radius at the corresponding in-plane wavevector. **c**, The complex eigenvalues return to their ini-

-tial positions at the end of the loop (namely, the blue dot and the red dot come back to themselves) when the system parameters come back to point A. **d,e,f**, Another loop is created $(A' \rightarrow B' \rightarrow C' \rightarrow D' \rightarrow A')$, which encloses an EP of the system (the same point $\mathrm{E_p}$ as in **a**). Following this new loop, the two eigenvalues switch their positions at the end of the loop (namely, the blue dot and the red dot switch their positions) when the system parameters come back to point A'. **g,h**, The two complex eigenvalues always switch their positions when we choose the right loops along other directions in the momentum space (Γ to N in **g** and Γ to M in **h**).

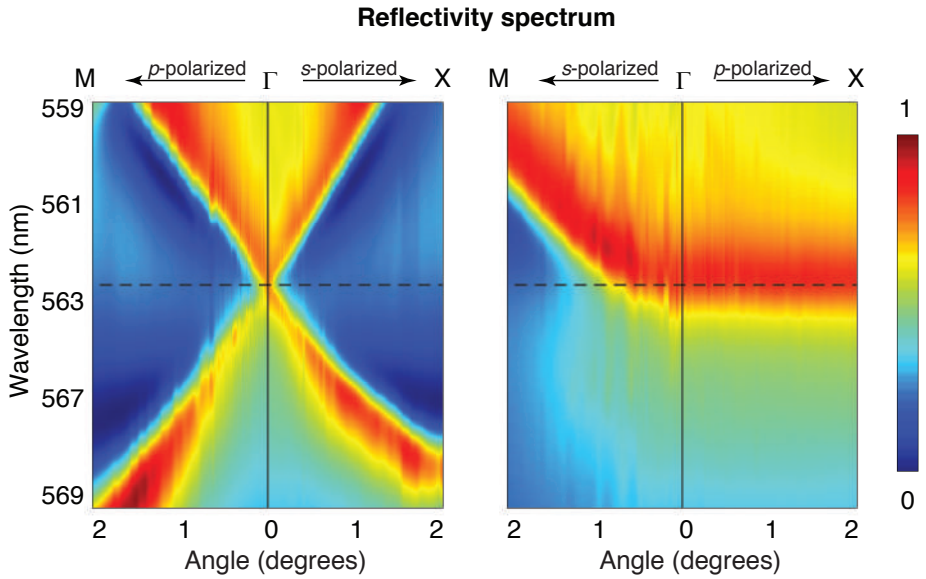

Supplementary Figure 4: **Experimental results of reflectivity showing an accidental Dirac cone.** Light with different polarizations (s and p) is selected to excite different resonances of the PhC slab along different directions in the k space. Depending on the choice of polarization, the two bands forming the conical dispersion are excited (s-polarized along Γ-X and p-polarized along Γ-M, shown in the left panel), or the flat band in the middle is excited (p-polarized along Γ-X and s-polarized along Γ-M, shown in the right panel).

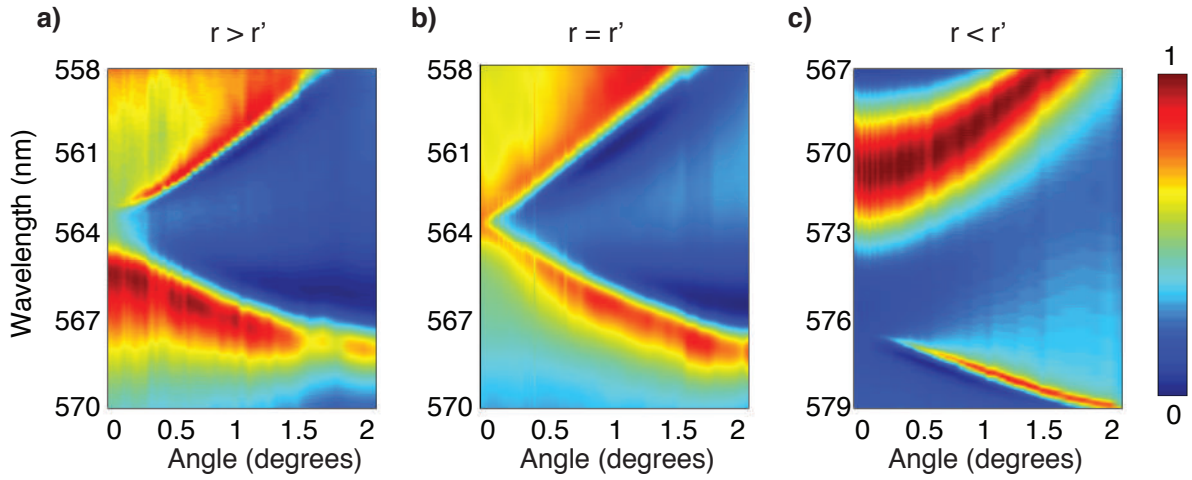

Supplementary Figure 5: **Experimental results of reflectivity from PhC slabs with and without accidental degeneracy.** Angle-resolved reflectivity along the Γ to X direction, measured for three different PhC slabs: **a**, with bigger hole radius than the structure with accidental degeneracy ($r > r'$); **b**, with accidental degeneracy ($r = r'$); **c**, with smaller hole radius than the structure with accidental degeneracy ($r < r'$). The reflectivity peaks of the structures without accidental degeneracy (**a,c**) follow quadratic dispersions; while the reflectivity peaks of the structure with accidental degeneracy (**b**) follow linear Dirac dispersion. Data shown in **b** is the same data as in Fig. 2c and the left panel of Fig. S3.

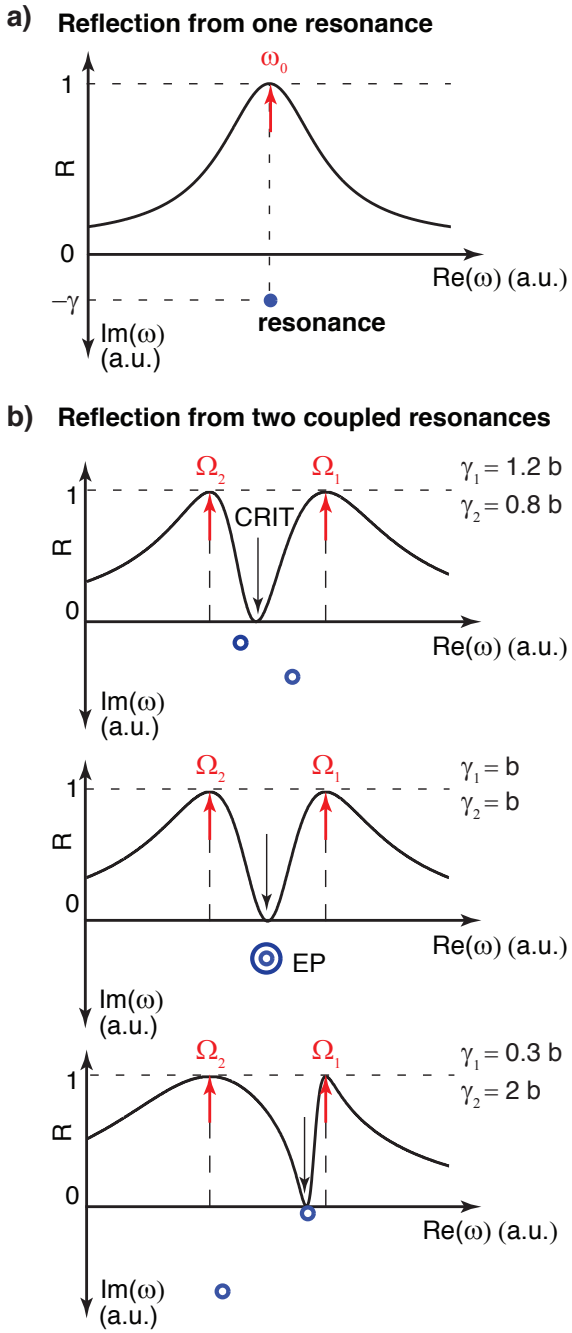

Supplementary Figure 6: **Illustrative reflectivity spectrum from one resonance and from two coupled resonances. a**, When a single resonance dominates, the reflectivity peak is at the same position as the real part of the complex eigenvalue. **b**, With two coupled resonances, the reflectivity peaks (red arrows) no longer follow the eigenvalues of the system (blue circles). As we vary the radiation loss $\gamma_{1,2}$ of the two resonances while fixing the eigenvalues $\Omega_{1,2}$ of the Hermitian matrix, we see the complex eigenvalues vary, whereas the reflectivity peaks are fixed. The middle panel of (b) shows a situation when the two complex eigenvalues coalesce into an EP.

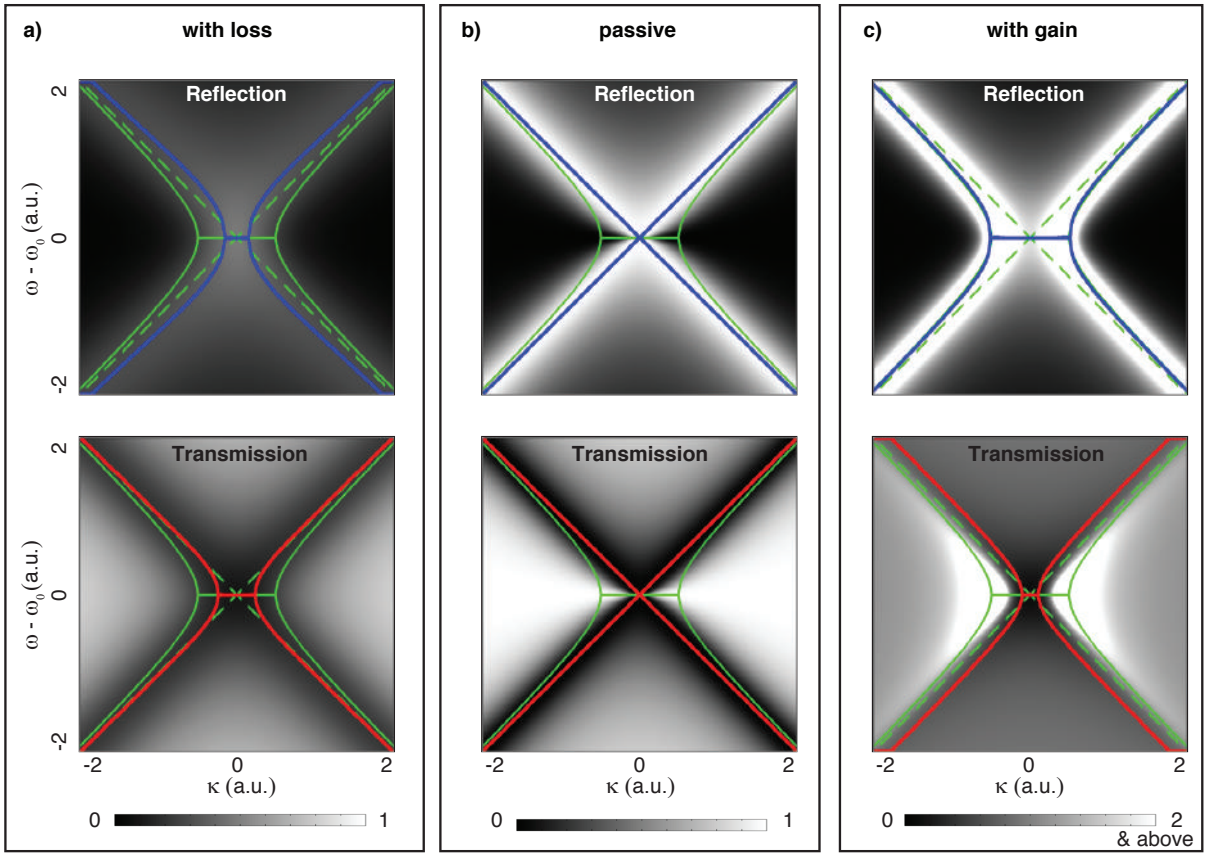

Supplementary Figure 7: **Effect of material loss and gain on the reflection and transmission spectra.** Reflection spectra (upper panels) and transmission spectra (lower panels) are plotted for three systems with the same radiation losses, but different material gain/loss: with material loss (**a**), purely passive with no gain or loss (**b**), and with material gain (**c**). For the purely passive system (**b**), the reflection peak (blue solid line) and the transmission dip (red solid line) correspond to the eigenvalue of the Hermitian part of the Hamiltonian (green dashed line), and show the linear Dirac dispersion. When material loss (**a**) or gain (**c**) is added to the system, the reflection peaks and transmission dips deviate from the linear Dirac dispersion and show branching behavior instead. The system parameters are given in Section VIII.

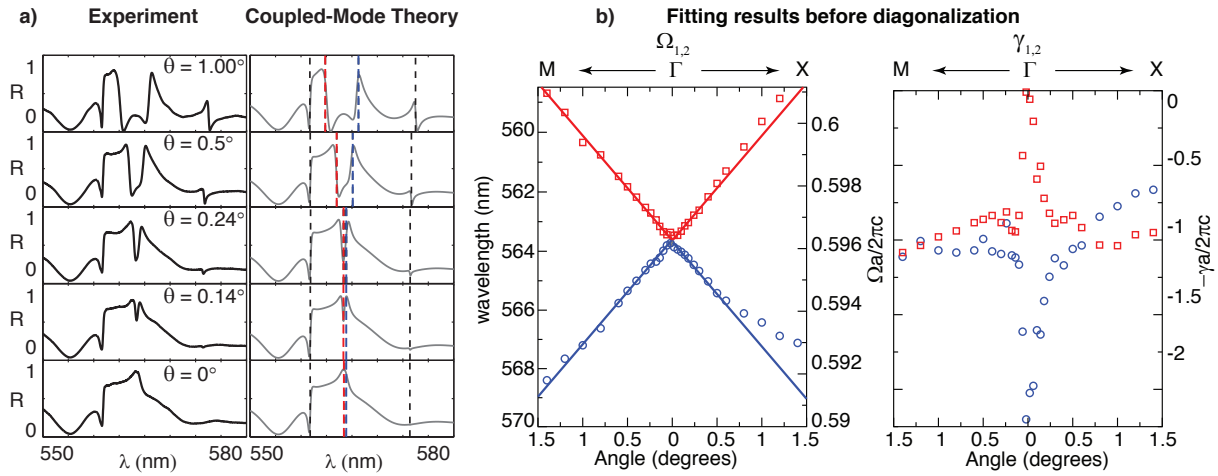

Supplementary Figure 8: **TCMT fitting and visualization of accidental Dirac cone. a**, Examples of reflection spectrum measured at five different incident angles (0°, 0.14°, 0.24°, 0.5° and 1°) along the Γ-X direction for s polarization, with comparison to the TCMT expression in equation (S.20) after fitting. Dotted lines indicate the resonances, with the two relevant resonances marked in red and blue. **b**, Parameters obtained from the TCMT fitting. The eigenvalues for the Hermitian part of the Hamiltonian, $\Omega_{1,2}$, are shown in the left panel and reveal the Dirac dispersion arising from accidental degeneracy. The diagonal terms for the anti-Hermitian part of the Hamiltonian, $\gamma_{1,2}$, are shown in the right panel. Note that the anti-Hermitian part of the Hamiltonian also has off-diagonal terms, so $\Omega_{1,2}$ and $\gamma_{1,2}$ are not the eigenvalues of the Hamiltonian. The eigenvalues of the Hamiltonian are shown in Fig. 3 of the main text.